Open Ceramics 8 (2021) 100198

Contents lists available at ScienceDirect

Open Ceramics

journal homepage: www.sciencedirect.com/journal/open-ceramics

Improved thermoelectric properties in ceramic composites based on $Ca_3Co_4O_9$ and $Na_2Ca_2Nb_4O_{13}$

R. Hinterding [a,*], M. Wolf [a], M. Jakob [b], O. Oeckler [b], A. Feldhoff [a,**]

[a] Leibniz University Hannover, Institute of Physical Chemistry and Electrochemistry, Callinstr. 3A, D-30167, Hannover, Germany
[b] Leipzig University, Institute of Mineralogy, Crystallography and Materials Science, Scharnhorststr. 20, D-04275, Leipzig, Germany

ARTICLE INFO

Keywords:
Calcium cobalt oxide
Composite
Ceramic
Sodium calcium niobate
Reaction sintering
Thermoelectrics
Power factor
Figure-of-merit

ABSTRACT

The oxide materials $Ca_3Co_4O_9$ and $Na_2Ca_2Nb_4O_{13}$ were combined in a new ceramic composite with promising synergistic thermoelectric properties. Both compounds show a plate-like crystal shape and similar aspect ratios but the matrix material $Ca_3Co_4O_9$ with lateral sizes of less than 500 nm is about two orders of magnitude smaller. Uniaxial pressing of the mixed compound powders was used to produce porous ceramics after conventional sintering. Reactions between both compounds and their compositions were thoroughly investigated. In comparison to pure $Ca_3Co_4O_9$, mixing with low amounts of $Na_2Ca_2Nb_4O_{13}$ proved to be beneficial for the overall thermoelectric properties. A maximum figure-of-merit of $zT = 0.32$ at 1073 K and therefore an improvement of about 19% was achieved by the ceramic composites.

1. Introduction

1.1. Thermoelectric energy harvesting

Energy harvesting is a topic with great significance to a mindful handling of limited resources. One possible route is the utilization of the thermoelectric effect to convert thermal energy into electrical energy. Apart from the aspects of processing and optimization of thermoelectric generators, the thermoelectric performance of the underlying materials still needs to be improved. Many different material classes are relevant in thermoelectrics, which differentiate in maximum efficiency, electrical power output, optimum temperature, chemical stability or toxicity. Among the most promising there are tellurides [1], half-Heusler compounds [2], Zintl phases [3], polymers [4], oxides [5] and oxyselenides [6]. Discussing the performance of thermoelectric materials requires the introduction of the fundamental thermoelectric material tensor in Eq. (1) [7–9].

$$\begin{pmatrix} I_q \\ I_S \end{pmatrix} = \frac{A}{L} \begin{pmatrix} \sigma & \sigma\cdot\alpha \\ \sigma\cdot\alpha & \sigma\cdot\alpha^2 + \Lambda \end{pmatrix} \cdot \begin{pmatrix} \Delta\varphi \\ \Delta T \end{pmatrix} \quad (1)$$

The tensor shows the coupling of currents of electrical charge I_q and entropy I_S for the energy conversion in a thermoelectric material with a cross-sectional area A and a length L [9]. The electrical potential difference $\Delta\varphi$ and the temperature difference ΔT may cause a thermally-induced electrical current, which is dependent on the three material parameters: the isothermal electrical conductivity σ, the Seebeck coefficient α and the electrically open-circuited entropy conductivity Λ. The more fundamental entropy conductivity is related to the open-circuited heat conductivity λ as shown in Eq. (2). Both terms can be condensed by using the term thermal conductivity [10].

$$zT = \frac{\sigma\cdot\alpha^2}{\lambda}\cdot T = \frac{\sigma\cdot\alpha^2}{\Lambda} = \frac{PF}{\Lambda} \quad (2)$$

The thermoelectric parameters all reappear in Eq. (2), where the performance of a thermoelectric material is given by the figure-of-merit zT. While the zT rules over the maximum energy conversion efficiency, the power factor $PF = \sigma \cdot \alpha^2$ is proportional to the maximum power output of a thermoelectric material. Both quantities are important to describe the thermoelectric performance of a material [10].

1.2. Composite materials

Specific single phase properties can be combined within a composite material. Depending on the characteristics of the combined materials, they can either coexist or interact with each other. Some theoretical limits of a coexisting two-phase composite were stated by Bergman et al.

* Corresponding author.
** Corresponding author.
E-mail addresses: richard.hinterding@pci.uni-hannover.de (R. Hinterding), armin.feldhoff@pci.uni-hannover.de (A. Feldhoff).

https://doi.org/10.1016/j.oceram.2021.100198
Received 6 May 2021; Received in revised form 20 October 2021; Accepted 4 November 2021
Available online 19 November 2021

[11]. The figure-of-merit zT of the single phase components shall not be exceeded by the composites, although it is possible concerning the power factor [12]. However, these studies do not take the more recently investigated interactions on the nanoscale into account. Furthermore, the transferability to a multiphase system is uncertain, which could be created by reactions between the mixing partners. The addition of one or multiple phases generally leads to heterointerfaces, which can decrease the mean-free path of phonons and thus reduce the thermal conductivity [13–15]. Note that depending on the additional phase, the overall thermal conductivity is not necessarily enhanced [16]. Mixing organic polymers and inorganic materials could improve the Seebeck coefficient effectively [17–19]. For $Ca_3Co_4O_9$ (CCO) in particular, Ag inclusions have proven to positively influence the thermoelectric performance [20–22]. Other metallic additions such as Co particles were beneficial for porous CCO systems by increasing the power factor [23]. Further adding polymers to a CCO/Ag system could reduce the thermal conductivity, but led to problems concerning the application temperature [24]. The power factor of a CCO composite was also increased by utilizing high dopant levels of Ca and Bi leading to a triple-phase composite [25]. Another study investigating the influence of adding La_2NiO_4 to a CCO matrix also revealed improved thermoelectric properties [26].

The present study investigates the influence on the thermoelectric properties of adding $Na_2Ca_2Nb_4O_{13}$ (NCNO) into a CCO matrix. CCO functions as the matrix material as it is well-known for its excellent thermoelectric properties. Furthermore, it is stable up to 1198 K in air [5,27], which makes it suitable for high-temperature applications. The thermoelectric properties of CCO are directly linked to its layered structure built up from two incommensurate subsystems [28]. CoO_2 constitutes one subsystem with a misfit-layered CdI_2 structure type while the other subsystem consists of three Ca_2CoO_3 units as a layered cutout of the rock-salt type [28]. Both subsystems alternate along the shared c-axis with same a and distinct b lattice parameters [29]. The layered structure results in strongly anisotropic thermoelectric properties [30,31]. NCNO on the other hand is mainly investigated with respect to the flux synthesis of single crystals [32] and its photocatalytic activity [33]. Structurally, the NCNO consists of $[(Ca_2Na)Nb_4O_{13}]^-$ perovskite-type layers linked by Na^+ cations [34,35]. The structure can be categorized as a Ruddlesden-Popper type and belongs to the Dion-Jacobson series of $Na[Ca_2Na_{n-3}Nb_nO_{3n+1}]$. The Na located between the layers should have a higher mobility and could therefore interact with the CCO during sintering. The obvious reason for NCNO not being used for thermoelectrics is the large bandgap of 3.3 eV [33], which results in electronically insulating characteristics. On the other hand, the inversely coupled Seebeck coefficient should be considerably large and surpass the one of CCO. Hence, an increased Seebeck coefficient and a decreasing electrical conductivity were expected from introducing NCNO into a CCO matrix with unknown consequences on the figure-of-merit. The usage of large plate-like particles of NCNO also allowed a preferred orientation during the uniaxial pressing. The final goal of preparing these CCO/NCNO ceramics was the improvement of the thermoelectric properties in comparison to pure CCO. To evaluate these properties, two different Ioffe plots with respect to the power factor and the entropy conductivity were applied [10,36].

2. Experimental

2.1. Materials

The composite materials were obtained by combining two different oxide powders. The oxide material $Ca_3Co_4O_9$ (CCO) functioned as a matrix and was purchased from CerPoTech (Tiller, Norway). The additive oxide material was $Na_2Ca_2Nb_4O_{13}$ (NCNO), which was synthesized by a molten-flux synthesis based on research from Arney et al. [33]. A stoichiometric mixture of water-free Na_2CO_3, $Ca(NO_3)_2 \cdot 4\ H_2O$ and Nb_2O_5 was mixed in a mortar and grinded for about 15 min. Afterwards, Na_2SO_4 was added in a 20:1 flux-to-reactant molar ratio and grinded again for about 15 min. The mixture was transferred into an alumina crucible and heated to 1373 K with a heating rate of 0.8 K/min in a muffle furnace. After a 10 h holding time, it was cooled to room temperature with a rate of 2 K/min. The white product powder was washed with hot deionized water in an ultrasonic bath to remove the flux and smaller particles. Ceramic composites containing CCO and NCNO were synthesized by grinding the precursor powders in a mortar for about 15 min with the respective weight ratios of 99:1, 95:5, 90:10 and 80:20 and a total weight of 1 g. The mixture was uniaxially pressed in a 16 mm steel die with 250 MPa at room temperature in air. Sintering was performed at ambient pressure at 1173 K for 10 h with a heating and cooling rate of 2 K min^{-1} in air. For thermoelectric measurements, the sintered disks were cut into bars with a length of 10 mm by using a precision vertical diamond wire saw from O'Well model 3242.

2.2. Analysis of microstructure

Phase purity of powders and ceramics was investigated by X-ray diffraction (XRD, Bruker AXS GmbH, Bruker D8 Advance) measurements, which were operated at 40 kV and 40 mA with Cu-K_α radiation. Powder diffraction data for identification and comparison within this work are used for the compounds $Ca_3Co_4O_9$ (Miyazaki et al. [29], monoclinic, a = 4.834 Å, b_1 = 2.824 Å, b_2 = 4.558 Å, c = 10.844 Å), $Na_2Ca_2Nb_4O_{13}$ (PDF: [01-089-6576], orthorhombic, a = 5.474 Å, b = 5.510 Å, c = 36.151 Å), $CaNbO_3$ (PDF: [01-089-0718], orthorhombic, a = 5.448 Å, b = 5.526 Å, c = 7.758 Å). The approach of a four-dimensional superspace group was used for CCO due to its incommensurate structure. Therefore, indexing of CCO in XRDs was realized with the superspace group Cm (0 1 - p 0) (equivalent to Bm (0 0 γ)) in accordance with literature [29,37,38]. A field-emission scanning eletron microscope (FE-SEM, JEOL JSM-6700F) was used for secondary electron micrographs of the powders at 2 kV. Elemental mappings were measured at 15 kV with with another FE-SEM (JEOL JSM-7610FPlus) equipped with two energy dispersive X-ray spectrometers (EDXS, Bruker, XFlash 6/60). Quantifications of elemental mappings were evaluated by the software Esprit version 2.2 from Bruker using the ZAF correction method. In-depth analysis of the composition was accomplished by a field-emission transmission electron microscope (TEM, JEOL JEM-2100F-UHR), which was also equipped with an EDXS (Oxford Instruments, INCA-300). Scanning TEM (STEM), high-resolution TEM (HRTEM) and selected area electron diffraction (SAED) were performed at 200 kV. Density and porosity of the sintered disks were determined by the Archimedes method (ISO 5018:1983). Isopropanol was used as a fluid and density values were averaged for three different disks.

2.3. Analysis of thermoelectric properties

Measurements of the electrical conductivity, Seebeck coefficient and heat conductivity were realized with respect to temperature dependency and orientation of the samples. The sintered ceramics were cut into bars (10 mm, 2 mm, 1.6 mm) to measure the electrical conductivity and the Seebeck coefficient perpendicular to the pressing direction. The measurement of the electrical conductivity was accomplished by a 4-point probe method at equilibrium conditions within a horizontal three-heating-zone tube furnace from Carbolite Gero EVZ 12/450B. The samples were heated to 1073 K with a heating rate of 3 K min^{-1} and maintained at this temperature for 4 h. Afterwards, the temperature program included cooling steps of 100 K with a dwell time of 2 h up to 873 K and 1 h up to 373 K. In total, the samples were exposed to a temperature above 373 K for more than 20 h. To measure the Seebeck coefficient, a ProboStat A setup from NorECs with a vertical furnace from Elite Thermal Systems Ltd. was used. Measurements were done with KEITHLEY multimeters and gained data processed by using Lab VIEW software. To gain values at equilibrium conditions, the temperature program included heating to 1073 K with a heating rate of 3 K min^{-1} and cooling steps of 100 K with dwell times of 1.5 h up to 773 K and 2 h

up to 373 K. A laser flash setup LFA 1000 from Linseis with an InSb detector was used to measure the thermal diffusivity D. Under helium (standard conditions), CCO started decomposing between 773 K and 873 K by releasing oxygen in accordance with literature [39]. Therefore, an oxygen-helium mixed atmosphere (20% O_2, 80% He) was used and values were averaged for three subsequent heating and cooling cycles to gain reliable data. Heat capacity c_p of each composite was measured in comparison to a pure CCO sample via the equations $\Delta T = E \cdot m^{-1} \cdot c_p^{-1}$ (ΔT = temperature difference in K; E = energy in J; m = mass of the sample in g; c_p = heat capacity in J g^{-1} K^{-1}) and $c_{p,sample} = c_{p,reference} \cdot \Delta T_{reference} \cdot m_{reference}$. Values for c_p of CCO were taken from literature [25]. Two different sample orientations i.e. perpendicular and parallel to the pressing direction were investigated. The measurements perpendicular to the pressing direction were conducted up to 573 K. Values of thermal diffusivity above 573 K with orientation perpendicular to the pressing direction were estimated by calculating polynomial fits for the measurements parallel to the pressing direction (compare another study using this method for more information [26]). As these parallel measurements were conducted in the full temperature range of 373 K to 1073 K, their calculated fits were transferred to the measurements in the other direction assuming similar trends with respect to the temperature.

3. Results and discussion

3.1. Compound powders

Two oxide powders with large differences in crystal sizes were used as base materials for the composites. As shown in Fig. 1, the CCO matrix powder was characterized by small particles with a plate-like shape. Its lateral extensions were about 200–500 nm and its thickness about 30 nm. The additive NCNO on the other hand showed the crystal morphology of microsheets with lateral extensions of up to 80 μm and a thickness of up to 8 μm. Therefore, both phases had a similar aspect ratio around 10 but were distinguished by two to three orders of magnitude respecting their crystal size. The small particle size of the CCO qualified it as a suitable matrix material for embedding the second phase. The plate-like crystal shape of both phases facilitate a preferred orientation when pressed, which can result in an ceramic with anisotropic transport properties.

3.2. Ceramic composite: composition and microstructure

The composition of the CCO/NCNO ceramic composites after sintering was investigated by XRD. For the NCNO compound powder, the sintered CCO and the sintered composites XRD patterns are displayed in Fig. 2. For the samples with low amounts of weighed NCNO (1 and 5 wt %), only the reflections for the matrix material CCO are visible. However, for the samples with 10 wt% and 20 wt% weighed NCNO, reflections of $CaNbO_3$ (CNO) became apparent. Since the original reflections of NCNO are not detected anymore, a reaction to CNO accompanied by a segregation of sodium is reasonable. The XRD patterns give no hint about a third phase containing sodium in the composites, although it could be nanocrystalline, only formed in minor amounts or integrated in the CCO matrix.

The formed CNO phase was further analyzed by SEM-EDXS in Fig. 3 for the sample with 5 wt% NCNO (compare Fig. S1 for an overview mapping). One single CNO particle is shown within the CCO matrix to analyze its composition. A morphological transformation at least at the surface of the particle is evident, which is now irregularly shaped. This is most likely due to reaction sintering and the newly formed phase. The EDX spectrum in Fig. 3b and the elemental distributions in Fig. 3d–h shows that the particles mainly consist of Ca, Nb and O, but also some Co and residual Na are noticeable. In the original NCNO, the Ca:Nb ratio is presumably 1:2 but in CNO it is 1:1, which means there should be an excess of Nb. The EDXS results suggest an even lower Ca:Nb ratio of 1:0.76 and therefore a segregation of Nb. There are no Nb-rich inclusions

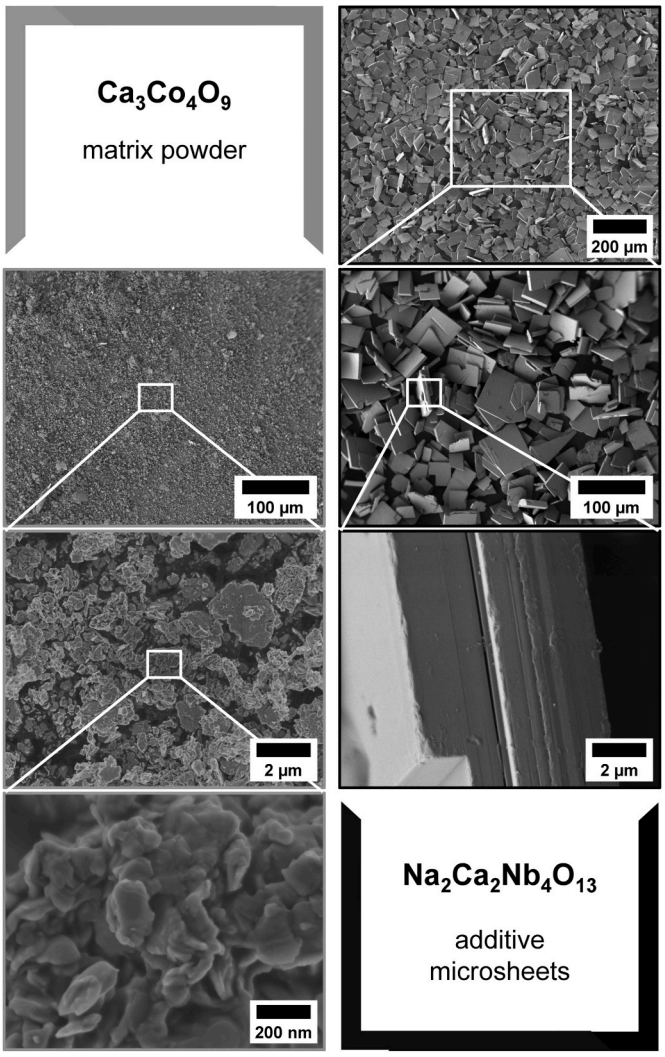

Fig. 1. SEM micrographs of the precursors powders $Ca_3Co_4O_9$ and $Na_2Ca_2Nb_4O_{13}$ used for the ceramic composites.

around the particle, but the surrounding CCO shows small amounts of approximately 1 at% Nb. This could mean that an integration of excess Nb into the CCO has occurred by exchanging Co from the CCO into the CNO particle. This cation exchange of $Co^{2+}/Co^{3+}/Co^{4+}$ and Nb^{5+} seems reasonable when the ionic radii are compared. For a coordination number of 6 (Co positions in CCO), the ionic radii are 65/55/53 pm for Co^{2+}(low-spin)/Co^{3+}(low-spin)/Co^{4+}(high-spin) and 64 pm for Nb^{5+} [40]. Based on the two subsystems of CCO, all three different valences occur, but the average value is between +3 and +4 in dependence of the variable oxygen amount [41,42]. The CoO_2 subsystem only features Co^{3+} and Co^{4+}, while the Ca_2CoO_3 contains Co^{2+} to some extent [43]. Comparing the ionic radii of Co and Nb ions, the substitution of Co^{2+} seems favored. However, substitution experiments involving Mn^{3+} (65 pm) or Fe^{2+} (61 pm) ions with similar radii to Nb^{5+} resulted in the substitution of Co^{3+} or Co^{4+} [42]. Investigations concerning Nb doping of CCO assume the same behavior [44]. Therefore, a substitution is clearly possible in this case, but the position is uncertain. The different charges of the ions suggest that the presence of oxygen is also essential for the cation exchange. The Ca:Co ratio in the CNO is 1:0.37 and together with the Nb amount this fits to $Ca(Nb,Co)O_3$ as the newly formed phase. Residual Na is left with a Ca:Na ratio of 1:0.12 and is most likely located on the Ca-position of the CNO. The Na within the original NCNO, which is partly located in between the NbO_6 octahedra, can be removed to gain the perovskite structure. This is well investigated for

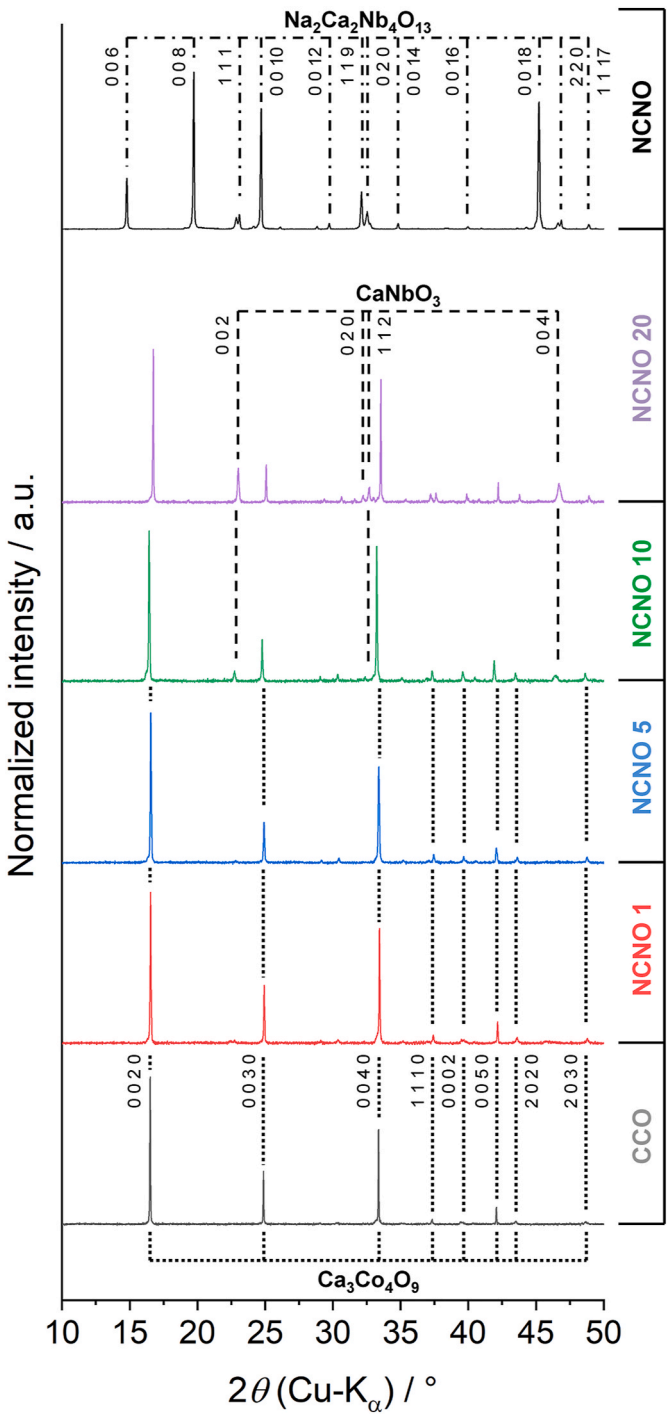

Fig. 2. XRD patterns of the compound NCNO powder, the sintered CCO/NCNO ceramic composites and the sintered CCO. All patterns were background-corrected and normalized for an easy comparison. Original phases of CCO and NCNO were indexed as well as the newly formed $CaNbO_3$. Reflections of the CCO were indexed with the four-dimensional superspace group approach [29,38].

the Dion-Jacobson series of $A[Ca_2Na_{n-3}Nb_nO_{3n+1}]$ in terms of ion intercalation and production of perovskite nanosheets [45–48]. Here, the introduction of Co and the high temperature during sintering could be the reason for the phase transformation. The structurally different atom positions of Na could also explain why there is still some Na left in the newly formed CNO. It is not entirely clear in which form the segregated Na remains, but the overview EDXS mapping in Fig. S1 suggests the formation of CoO containing Na and Ca to some extent. The main observations during the sintering were summarized and illustrated by the reaction scheme given in Fig. 4.

Further analysis regarding the newly formed CNO was performed by TEM measurements in Fig. 5. The cross-section of a former NCNO plate and the respective EDXS mapping are given in Fig. 5a,d. The irregular shape at the surface and the introduction of Co into the CNO as found in the SEM results can be recognized. The elemental distribution of Ca, Co and Nb is also rather homogeneous within the CNO particle. The CCO plate crossing the CNO particle also shows a loss of Co and a gain of Nb, resulting in a Ca:Co ratio of 1.08 and a Ca:Nb ratio of 1:0.17. This supports the assumption of a cation exchange between the CCO and the NCNO as the Ca:(Co,Nb) ratio is at 1:1.25 and therefore close to the original Ca:Co ratio of 1:1.33. Again, no new phase with Na as a major element was found in the close vicinity of the CNO particle. EDXS showed only trace amounts of Na within the CNO and no Na within the CCO particle. Therefore, the Na is most likely located within some CoO in the CCO matrix as suggested by Fig. S1 or evaporated to some extent during sintering. The CNO phase was also investigated by SAED and HRTEM for the zone axes [112] in Fig. 5b and c and for [001] in Fig. 5e and f. Both zone axes gave a clear diffraction pattern at the marked location of Fig. 5a, which allowed the distinct indexing of them. As not the whole particle was oriented simultaneously, polycrystallinity seems reasonable. Furthermore, the [001] orientation in Fig. 5f allowed the determination of the *a*- and *b*-axis lattice parameters (5.57 Å and 5.66 Å respectively), which are only slightly larger than the literature data for pure $CaNbO_3$ (5.45 Å and 5.53 Å respectively for ICSD 01-089-0718).

3.3. Ceramic composite: thermoelectric properties

The microstructure analysis in section 3.2 revealed that CCO and NCNO do not coexist at high temperatures and the formation of CNO is induced with the loss of Na. The influence of the new phases within the CCO matrix was investigated by measuring the electrical conductivity σ, Seebeck coefficient α and heat conductivity λ of the CCO/LNO ceramic composites in Fig. 6.

The electrical conductivity (see Fig. 6a) shows the expected decreasing trend with increasing amounts of NCNO. However, the sample with 1 wt% NCNO shows even slightly higher values and the 5 wt % only a small decrease. This behavior could be linked to the cation exchange between the CCO and NCNO, which leads to a Nb-doped CCO. A similar trend was found by Zhu et al. [44] for targeted Nb-doping of CCO, where low amounts of Nb lowered the electrical resistivity and higher amounts increased it. The decrease in electrical conductivity is also caused by the $Ca(Nb,Co)O_3$ phase, which originates from the $CaNbO_3$ with really low values of 10^{-5} S cm^{-1} at 750 K [49]. No significant or sudden changes of the electrical conductivity were observed during the measurement time of more than 20 h above 373 K for the composites as well as for the pure CCO. As uncomplete reactions can be an issue for the long-term stability of composites, these changes would be unfavorable. Based on the measurements, complete reactions and stable composites are suggested. More details about the electrical conductivity were observed by the Arrhenius plot in Fig. S3. A metallic-to-semiconducting transition between 573-673 K was found for CCO in accordance with literature [50,51]. For high temperatures, the composites also show an increase of the activation energy for the electronic transport, which is caused by hindered transport across the additional phases. The Seebeck coefficient is usually inversely coupled to the electrical conductivity, which is also the case for the investigated composites. The main reason for the increasing Seebeck coefficient is most likely the additional $Ca(Nb,Co)O_3$ phase within the system. Although no systematical studies of the electronic properties of the $Ca(Nb,Co)_3$ system and the consequences of substituting Nb with Co were available, the undoped $CaNbO_3$ and $CaCoO_3$ can give some information. On the one hand the $CaNbO_3$ shows *p*-type conductivity by a positive Seebeck coefficient and electrically insulating characteristics [49]. On

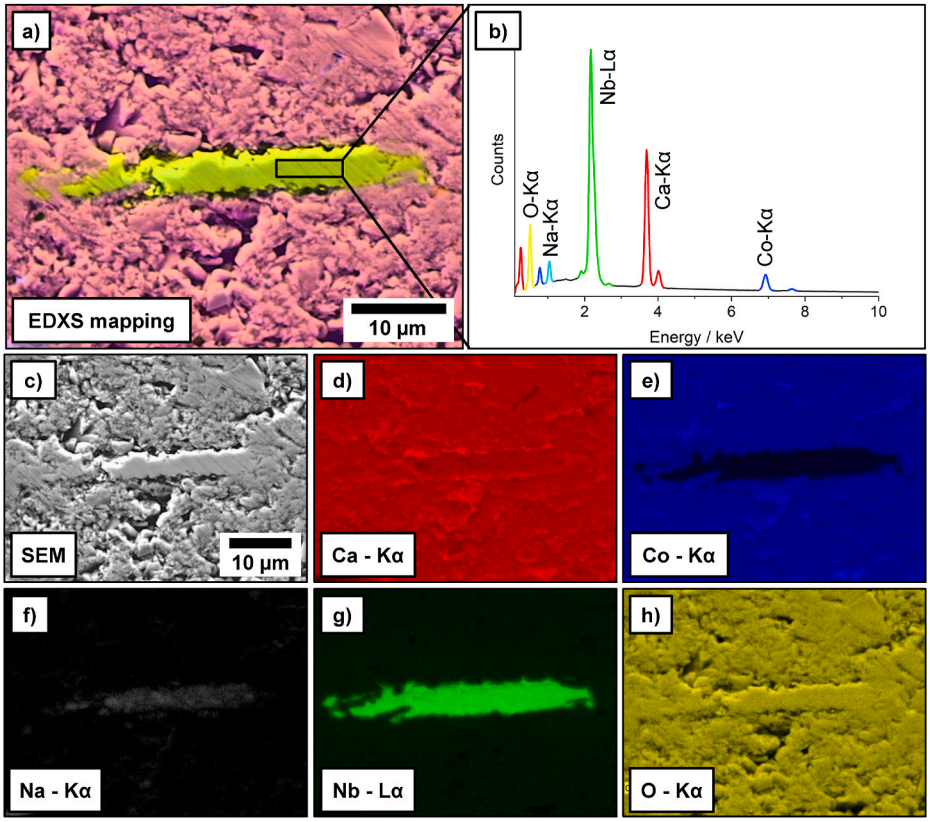

Fig. 3. Cross-sectional SEM-EDXS analysis of the 5 wt% NCNO sample after sintering showing a single CNO plate-like particle embedded in a CCO matrix. a) Overlay EDXS mapping summarizing the results from c-h. b) EDX spectrum shows exemplarily the composition of the CNO phase. c) SEM micrograph as basis for EDXS analysis. d-h) Elemental distributions of the respective elements Ca, Co, Na, Nb and O.

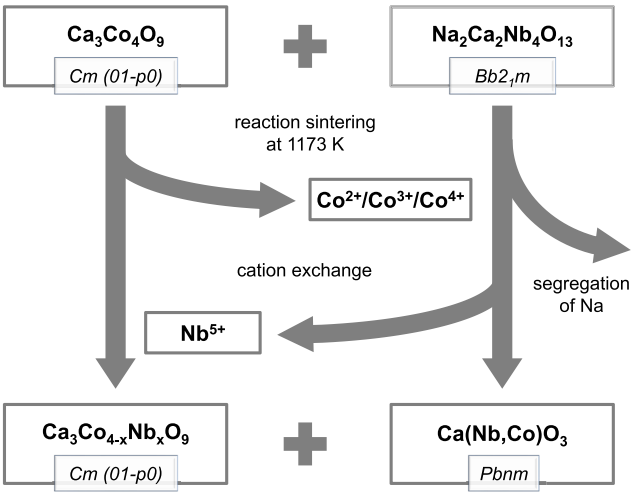

Fig. 4. Reaction scheme of CCO and NCNO during reaction sintering. A cation exchange between CCO and the newly formed $Ca(Co,Nb)O_3$ occurred and Na partly segregated.

the other hand the $CaCoO_3$ shows a nonmetallic behavior regarding the temperature dependency of the electrical conductivity despite showing large values of 333 S cm^{-1} at room temperature [52]. Therefore, a higher electrical conductivity but lower Seebeck coefficient of $Ca(Nb,Co)O_3$ in comparison to $CaNbO_3$ are reasonable. It should be noted that the amount of initial NCNO could also have an impact on the Nb:Co ratio and therefore the thermoelectric properties. This could explain why the sample containing 20 wt% NCNO shows a different slope than the samples containing less amounts. Another subordinate factor concerning the Seebeck coefficient is the introduction of Nb into the CCO, where a higher Nb amount led to increased values [53]. Combining the electrical conductivity and the Seebeck coefficient gives the power factor in Fig. 6c. The samples containing 1–10 wt% NCNO all show an increase, especially towards higher temperatures. The maximum value is reached by the 5 wt% sample and the decreasing electrical conductivity becomes prevalent for the 20 wt% sample. The last part for a complete picture of the thermoelectric properties is the thermal conductivity, which is given as the heat conductivity in Fig. 6d. All investigated ceramic composites showed a decreased heat conductivity for the whole temperature range. This could be caused by the additional phonon scattering sites coming from the $Ca(Nb,Co)O_3$ phase, but the larger atomic mass of Nb in comparison to Co and the Nb-doping could also play a significant role. Interestingly, the heat conductivity between the 1–10 wt% samples did not differ by much and shows if anything an increasing trend. This could be caused by a higher heat conductivity of the additional phase, which balances out with the increased phonon scattering at interfaces. It should be noted that the values of λ above 573 K were fitted to the measurements parallel to the pressing direction (compare Fig. S2). The reason for this was the applied oxygen-helium atmosphere, which did not allow higher temperatures with the used setup. A comparison of measurements for CCO in both directions from the literature validates this method, as the temperature dependent trend is comparable [30,54]. The same method was also used in a previous study investigating CCO composites [26]. By comparing the heat conductivity parallel and perpendicular to the pressing direction differences become obvious (compare Fig. S2), which are most likely caused by some anisotropy of the ceramic samples. This anisotropy comes from the preferred orientation of CCO and the CNO due to uniaxial pressing. This underlines the importance of combining the thermoelectric properties within the same

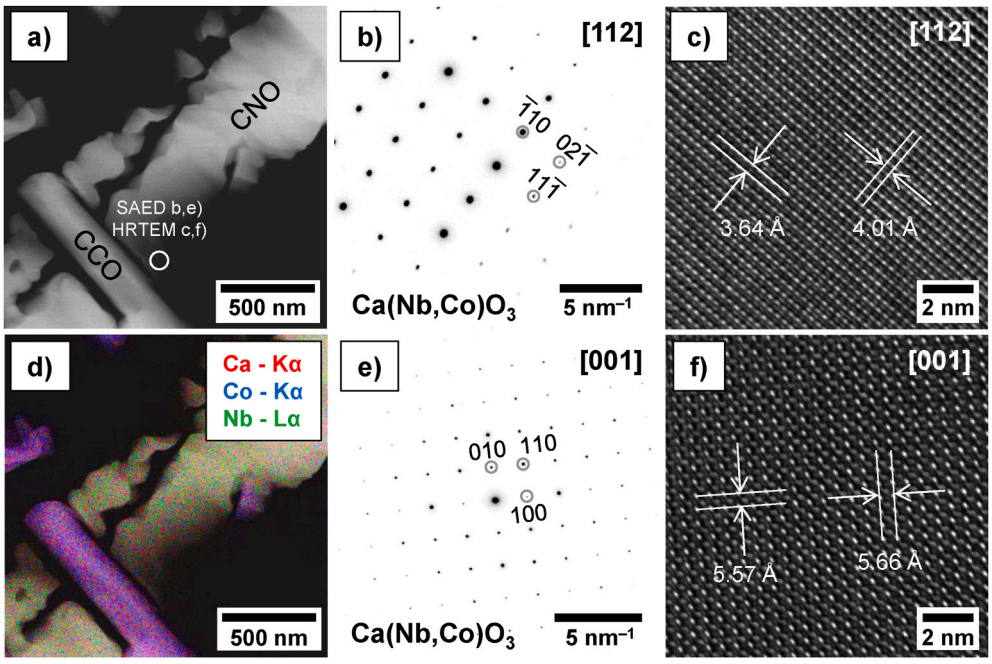

Fig. 5. Cross-sectional TEM characterization of the sample with 5 wt% NCNO. a,d) STEM annular dark-field micrograph of a large plate-like $Ca(Co,Nb)O_3$ (CNO) grain partly surrounded by CCO and the EDXS mapping of the CNO grain showing a homogeneous distribution of Ca and Nb as well as the introduction of Co. b,c,e,f) SAED pattern and corresponding high-resolution TEM micrographs along the [112] and the [100] zone axes of the newly formed CNO phase.

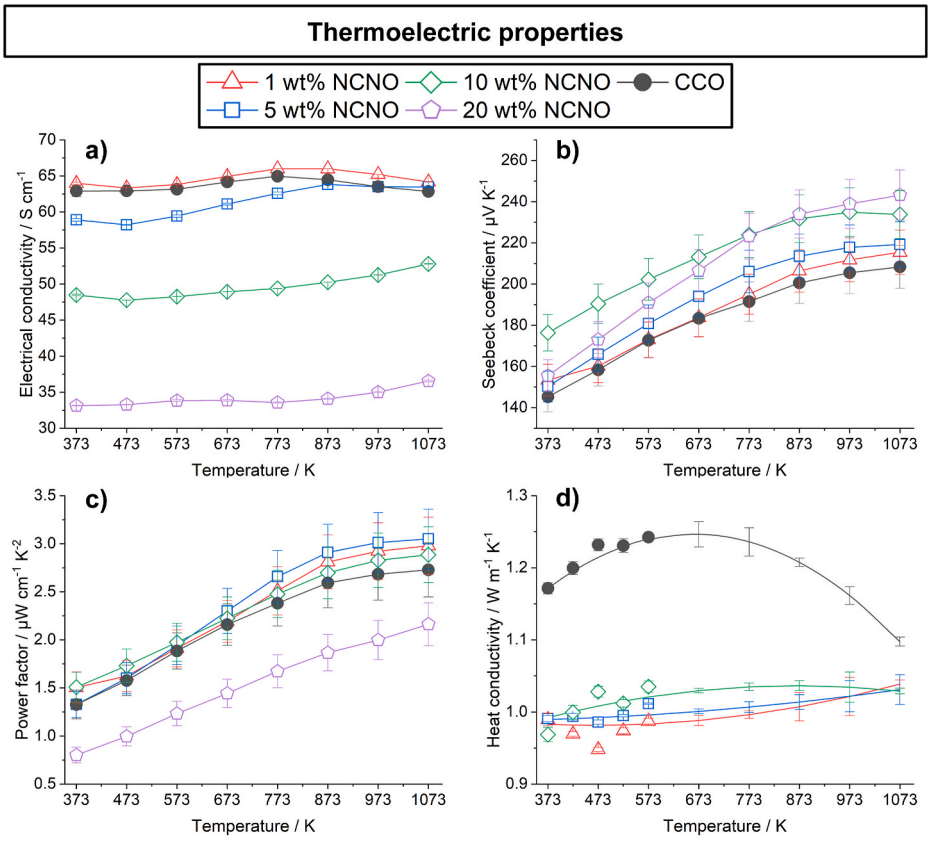

Fig. 6. Thermoelectric properties of the CCO/NCNO ceramic composites perpendicular to the pressing direction in dependence on temperature with standard deviations. a) Electrical conductivity with similar values for the 1 wt% and decreasing values for higher amounts of NCNO in comparison to CCO. b) Seebeck coefficient with increasing values for all ceramic composites. c) Power factor with increased values for all investigated composites except the 20 wt% NCNO sample. d) Heat conductivity with decreased values for the ceramic composites. Values above 573 K for the heat conductivity were gained by transferring fits and error bars for measurements parallel to the pressing direction (see Fig. S2).

direction.

Two different Ioffe plots and the figure-of-merit zT displayed in Fig. 7 were derived from the thermoelectric properties in Fig. 6. The type-I Ioffe plot in Fig. 7a gives the power factor in dependence of the electrical conductivity, which allows a clear comparison between the different samples. Increased power factors at high temperatures are noticed for the 1–10 wt% samples. The decreasing electrical conductivity correlates with the increasing Seebeck coefficient and becomes

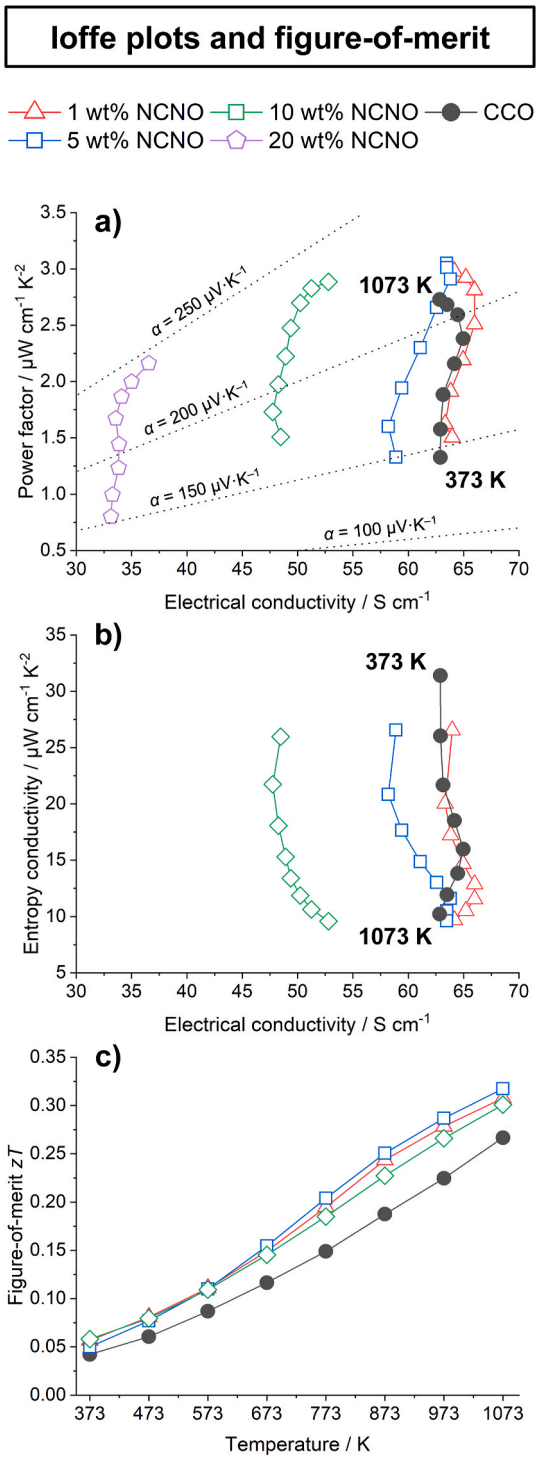

Fig. 7. Ioffe plots with 100 K temperature steps and figure-of-merit zT of the CCO/NCNO ceramic composites. a) Type-I Ioffe plot with the power factor against the electrical conductivity. The samples with 1 wt%, 5 wt% and 10 wt% NCNO show a higher power factor than the CCO. b) Type-II Ioffe plot with the entropy conductivity against the electrical conductivity. Slightly lower values were reached at high temperatures in comparison to pure CCO. c) Figure-of-merit zT against the temperature. All investigated composites show an increased average and maximum zT.

dominant for 20 wt% NCNO. The type-II Ioffe plot in Fig. 7b shows the thermal properties in terms of entropy conductivity Λ in dependence of the electrical conductivity. Slightly lower values at high temperatures were reached by the composites. Additionally, the maximum entropy conductivity could effectively be reduced for lower temperatures. Finally, the figure-of-merit zT was determined perpendicular to the pressing direction by combining the power factor and the entropy conductivity. The corresponding plot against the temperature is given in Fig. 7c. The samples with 1–10 wt% NCNO all show improved values with the 1 wt% and 5 wt% sample being the best. This results from the increased power factor and the simultaneously low entropy conductivity. The 1 wt% sample has a slightly lower figure-of-merit in comparison to the 5 wt%, but the electrical conductivity is higher. The difference of the figure-of-merit between composites with low amounts of NCNO and the pure CCO becomes more pronounced with increasing temperatures and reaches its maximum value at 1073 K with 0.32 against 0.27, which is equivalent to an improvement of approximately 19%.

4. Conclusions

Ceramic composites based on the undoped $Ca_3Co_4O_9$ and $Na_2Ca_2Nb_4O_{13}$ were produced with varying ratios between both compounds. Using undoped $Ca_3Co_4O_9$ allowed the determination of the reasons in changing thermoelectric properties, but future research could benefit further from a doped CCO. Analysis of the microstructure by XRD, SEM, EDXS and TEM suggested a cation exchange of Co and Nb between the matrix material and the additive material as well as a newly formed $Ca(Nb,Co)O_3$ phase. The Seebeck coefficient was increased for the ceramic composites but the electrical conductivity was reduced, with the exception of sample containing 1 wt% of the additive. Both values combined led to an improved power factor for the samples containing 1–10 wt% additive. The introduction of additional phases also led to a small reduction of the thermal conductivity. As a result, the maximum figure-of-merit zT at 1073 K was increased by about 19% for the composite with 5 wt% $Na_2Ca_2Nb_4O_{13}$ in comparison to pure $Ca_3Co_4O_9$. These results underline the potential of composite materials concerning improved thermoelectric properties.

Declaration of competing interest

The authors declare that they have no known competing financial interests or personal relationships that could have appeared to influence the work reported in this paper.

Acknowledgements

This work was supported by the Deutsche Forschungsgemeinschaft (DFG, German Research Foundation) - project number 325156807. Authors gratefully appreciate technical assistance by F. Steinbach.

Appendix A. Supplementary data

Supplementary data to this article can be found online at https://doi.org/10.1016/j.oceram.2021.100198.

References

[1] G. Tan, L.-D. Zhao, M.G. Kanatzidis, Rationally designing high-performance bulk thermoelectric materials, Chem. Rev. 116 (2016) 12123–12149, https://doi.org/10.1021/acs.chemrev.6b00255.
[2] S.J. Poon, Recent advances in thermoelectric performance of half-Heusler compounds, Metals 8 (2018) 989, https://doi.org/10.3390/met8120989.
[3] J. Shuai, J. Mao, S. Song, Q. Zhang, G. Chen, Z. Ren, Recent progress and future challenges on thermoelectric Zintl materials, Materials Today Physics 1 (2017) 74–95, https://doi.org/10.1016/j.mtphys.2017.06.003.
[4] Q. Zhang, Y. Sun, W. Xu, D. Zhu, Organic thermoelectric materials: emerging green energy materials converting heat to electricity directly and efficiently, Adv. Mater. 26 (2014) 6829–6851, https://doi.org/10.1002/adma.201305371.
[5] Y. Yin, B. Tudu, A. Tiwari, Recent advances in oxide thermoelectric materials and modules, Vacuum 146 (2017) 356–374, https://doi.org/10.1016/j.vacuum.2017.04.015.
[6] L.-D. Zhao, J. He, D. Berardan, Y. Lin, J.-F. Li, C.-W. Nan, N. Dragoe, BiCuSeO oxyselenides: new promising thermoelectric materials, Energy Environ. Sci. 7 (2014) 2900–2924, https://doi.org/10.1039/c4ee00997e.

[7] H.U. Fuchs, A direct entropic approach to uniform and spatially continuous dynamical models of thermoelectric devices, Energy.Harvest.Syst. 1 (2014), https://doi.org/10.1515/ehs-2014-0011.

[8] A. Feldhoff, Thermoelectric material tensor derived from the Onsager–de Groot–Callen model, Energy.Harvest.Syst. 2 (2015), https://doi.org/10.1515/ehs-2014-0040.

[9] A. Feldhoff, Power conversion and its efficiency in thermoelectric materials, Entropy 22 (2020) 803, https://doi.org/10.3390/e22080803.

[10] M. Wolf, R. Hinterding, A. Feldhoff, High power factor vs. high zT—a review of thermoelectric materials for high-temperature application, Entropy 21 (2019) 1058, https://doi.org/10.3390/e21111058.

[11] D.J. Bergman, O. Levy, Thermoelectric properties of a composite medium, J. Appl. Phys. 70 (1991) 6821–6833, https://doi.org/10.1063/1.349830.

[12] D.J. Bergman, L.G. Fel, Enhancement of thermoelectric power factor in composite thermoelectrics, J. Appl. Phys. 85 (1999) 8205–8216, https://doi.org/10.1063/1.370660.

[13] Q. Zhang, X. Ai, L. Wang, Y. Chang, W. Luo, W. Jiang, L. Chen, Improved thermoelectric performance of silver nanoparticles-dispersed Bi_2Te_3 composites deriving from hierarchical two-phased heterostructure, Adv. Funct. Mater. 25 (2015) 966–976, https://doi.org/10.1002/adfm.201402663.

[14] W. Liu, X. Yan, G. Chen, Z. Ren, Recent advances in thermoelectric nanocomposites, Nano Energy 1 (2012) 42–56, https://doi.org/10.1016/j.nanoen.2011.10.001.

[15] K. Kato, K. Kuriyama, T. Yabuki, K. Miyazaki, Organic-inorganic thermoelectric material for a printed generator, J. Phys. Conf. 1052 (2018), 012008, https://doi.org/10.1088/1742-6596/1052/1/012008.

[16] F. Delorme, P. Diaz-Chao, E. Guilmeau, F. Giovannelli, Thermoelectric properties of $Ca_3Co_4O_9$–Co_3O_4 composites, Ceram. Int. 41 (2015) 10038–10043, https://doi.org/10.1016/j.ceramint.2015.04.091.

[17] B. Zhang, J. Sun, H.E. Katz, F. Fang, R.L. Opila, Promising thermoelectric properties of commercial PEDOT:PSS materials and their Bi_2Te_3 powder composites, ACS Appl. Mater. Interfaces 2 (2010) 3170–3178, https://doi.org/10.1021/am100654p.

[18] N. Toshima, Recent progress of organic and hybrid thermoelectric materials, Synth. Met. 225 (2017) 3–21, https://doi.org/10.1016/j.synthmet.2016.12.017.

[19] M. Culebras, A. García-Barberá, J.F. Serrano-Claumarchirant, C.M. Gómez, A. Cantarero, Hybrids composites of NCCO/PEDOT for thermoelectric applications, Synth. Met. 225 (2017) 103–107, https://doi.org/10.1016/j.synthmet.2016.12.016.

[20] Y. Song, Q. Sun, L. Zhao, F. Wang, Z. Jiang, Synthesis and thermoelectric power factor of $(Ca_{0.95}Bi_{0.05})_3Co_4O_9$/Ag composites, Mater. Chem. Phys. 113 (2009) 645–649, https://doi.org/10.1016/j.matchemphys.2008.08.029.

[21] F. Kahraman, M.A. Madre, S. Rasekh, C. Salvador, P. Bosque, M.A. Torres, J. C. Diez, A. Sotelo, Enhancement of mechanical and thermoelectric properties of $Ca_3Co_4O_9$ by Ag addition, J. Eur. Ceram. Soc. 35 (2015) 3835–3841, https://doi.org/10.1016/j.jeurceramsoc.2015.05.029.

[22] Z. Shi, C. Zhang, T. Su, J. Xu, J. Zhu, H. Chen, T. Gao, M. Qin, P. Zhang, Y. Zhang, H. Yan, F. Gao, Boosting the thermoelectric performance of calcium cobaltite composites through structural defect engineering, ACS Appl. Mater. Interfaces 12 (2020) 21623–21632, https://doi.org/10.1021/acsami.0c03297.

[23] G. Constantinescu, A.R. Sarabando, S. Rasekh, D. Lopes, S. Sergiienko, P. Amirkhizi, J.R. Frade, A.V. Kovalevsky, Redox-promoted tailoring of the high-temperature electrical performance in $Ca_3Co_4O_9$ thermoelectric materials by metallic cobalt addition, Materials 13 (2020), https://doi.org/10.3390/ma13051060.

[24] M. Wolf, K. Menekse, A. Mundstock, R. Hinterding, F. Nietschke, O. Oeckler, A. Feldhoff, Low thermal conductivity in thermoelectric oxide-based multiphase composites, J. Electron. Mater. 48 (2019) 7551–7561, https://doi.org/10.1007/s11664-019-07555-2.

[25] M. Bittner, N. Kanas, R. Hinterding, F. Steinbach, D. Groeneveld, P. Wemhoff, K. Wiik, M.-A. Einarsrud, A. Feldhoff, Triple-phase ceramic 2D nanocomposite with enhanced thermoelectric properties, J. Eur. Ceram. Soc. 39 (2019) 1237–1244, https://doi.org/10.1016/j.jeurceramsoc.2018.10.023.

[26] R. Hinterding, Z. Zhao, M. Wolf, M. Jakob, O. Oeckler, A. Feldhoff, Ceramic composites based on $Ca_3Co_{4-x}O_{9+\delta}$ and $La_2NiO_{4+\delta}$ with enhanced thermoelectric properties, Open Ceramics 6 (2021) 100103, https://doi.org/10.1016/j.oceram.2021.100103.

[27] J.W. Fergus, Oxide materials for high temperature thermoelectric energy conversion, J. Eur. Ceram. Soc. 32 (2012) 525–540, https://doi.org/10.1016/j.jeurceramsoc.2011.10.007.

[28] Y. Miyazaki, Crystal structure and thermoelectric properties of the misfit-layered cobalt oxides, Solid State Ionics 172 (2004) 463–467, https://doi.org/10.1016/j.ssi.2004.01.046.

[29] Y. Miyazaki, M. Onoda, T. Oku, M. Kikuchi, Y. Ishii, Y. Ono, Y. Morii, T. Kajitani, Modulated structure of the thermoelectric compound $[Ca_2CoO_3]_{0.62}CoO_2$, J. Phys. Soc. Jpn. 71 (2002) 491–497, https://doi.org/10.1143/JPSJ.71.491.

[30] D. Kenfaui, B. Lenoir, D. Chateigner, B. Ouladdiaf, M. Gomina, J.G. Noudem, Development of multilayer textured $Ca_3Co_4O_9$ materials for thermoelectric generators: influence of the anisotropy on the transport properties, J. Eur. Ceram. Soc. 32 (2012) 2405–2414, https://doi.org/10.1016/j.jeurceramsoc.2012.03.022.

[31] S. Bresch, B. Mieller, D. Schoenauer-Kamin, R. Moos, F. Giovanelli, T. Rabe, Influence of pressure assisted sintering and reaction sintering on microstructure and thermoelectric properties of bi-doped and undoped calcium cobaltite, J. Appl. Phys. 126 (2019), 075102, https://doi.org/10.1063/1.5107476.

[32] S. Oishi, Y. Nagai, K. Chiba, N. Ishizawa, Growth of layered perovskite-type $Na_2Ca_2Nb_4O_{13}$ crystals by the Na_2SO_4 flux method, Chem. Lett. 27 (1998) 439–440, https://doi.org/10.1246/cl.1998.439.

[33] D. Arney, L. Fuoco, J. Boltersdorf, P.A. Maggard, Flux synthesis of $Na_2Ca_2Nb_4O_{13}$: the influence of particle shapes, surface features, and surface areas on photocatalytic hydrogen production, J. Am. Ceram. Soc. 96 (2013) 1158–1162, https://doi.org/10.1111/jace.12122.

[34] K. Chiba, Structure of layered perovskite-type $Na_2Ca_2Nb_4O_{13}$ single crystals, Solid State Ionics 108 (1998) 179–183, https://doi.org/10.1016/S0167-2738(98)00037-X.

[35] K. Chiba, N. Ishizawa, S. Oishi, A Ruddlesden–Popper-type layered perovskite, $Na_2Ca_2Nb_4O_{13}$, Acta Crystallogr. Sect. C Cryst. Struct. Commun. 55 (1999) 1041–1044, https://doi.org/10.1107/S0108270199001134.

[36] A.F. Ioffe, Semiconductor Thermoelements and Thermoelectric Cooling, first ed., Info-search Ltd., London, 1957.

[37] T. Janssen, A. Janner, A. Looijenga-Vos, P.M. De Wolff, International Tables for Crystallography Volume C: 9.8 Incommensurate and Commensurate Modulated Structures, vol. 3, Kluwer Acad. Publ, Dordrecht, 2004.

[38] T. Janssen, G. Chapuis, M. de Boissieu, Aperiodic Crystals: from Modulated Phases to Quasicrystals, Volume 20 of *International Union of Crystallography Monographs on Crystallography*, Oxford University Press, Oxford and New York, 2007.

[39] N. Kanas, G. Skomedal, T.D. Desissa, A. Feldhoff, T. Grande, K. Wiik, M.-A. Einarsrud, Performance of a thermoelectric module based on *n*-type $(La_{0.12}Sr_{0.88})_{0.95}TiO_{3-\delta}$ and *p*-type $Ca_3Co_{4-x}O_{9+\delta}$, J. Electron. Mater. 49 (2020) 4154–4159, https://doi.org/10.1007/s11664-020-08127-5.

[40] R.D. Shannon, Revised effective ionic radii and systematic studies of interatomic distances in halides and chalcogenides, Acta Crystallogr. A 32 (1976) 751–767, https://doi.org/10.1107/S0567739476001551.

[41] U. Hira, L. Han, K. Norrman, D.V. Christensen, N. Pryds, F. Sher, High-temperature thermoelectric properties of Na- and W-doped $Ca_3Co_4O_9$ system, RSC Adv. 8 (2018) 12211–12221, https://doi.org/10.1039/c8ra01691g.

[42] Y. Wang, Y. Sui, P. Ren, L. Wang, X. Wang, W. Su, H. Fan, Strongly correlated properties and enhanced thermoelectric response in $Ca_3Co_{4-x}M_xO_9$ (M = Fe, Mn, and Cu), Chem. Mater. 22 (2010) 1155–1163, https://doi.org/10.1021/cm902483a.

[43] S. Lambert, H. Leligny, D. Grebille, Three forms of the misfit layered cobaltite $[Ca_2CoO_3][CoO_2]_{1.62}$ · A 4D structural investigation, J. Solid State Chem. 160 (2001) 322–331, https://doi.org/10.1006/jssc.2001.9235.

[44] C. Zhu, H. An, W. Ge, Z. Li, G. Tang, Enhancing the thermoelectric properties of $Ca_3Co_4O_9$ thin films by Nb ion injection, J. Alloys Compd. 567 (2013) 122–126, https://doi.org/10.1016/j.jallcom.2013.03.069.

[45] M.M.J. Treacy, S.B. Rice, A.J. Jacobson, J.T. Lewandowski, Electron microscopy study of delamination in dispersions of the perovskite-related layered phases K $[Ca_2Na_{n-3}Nb_nO_{3n-1}]$: evidence for single-layer formation, Chem. Mater. 2 (1990) 279–286, https://doi.org/10.1021/cm00009a018.

[46] Y.-S. Han, I. Park, J.-H. Choy, Exfoliation of layered perovskite, $KCa_2Nb_3O_{10}$, into colloidal nanosheets by a novel chemical process, J. Mater. Chem. 11 (2001) 1277–1282, https://doi.org/10.1039/B006045N.

[47] B.-W. Li, M. Osada, Y.-H. Kim, Y. Ebina, K. Akatsuka, T. Sasaki, Atomic layer engineering of high-κ ferroelectricity in 2D perovskites, J. Am. Chem. Soc. 139 (2017) 10868–10874, https://doi.org/10.1021/jacs.7b05665.

[48] R. Hinterding, A. Feldhoff, Two-dimensional oxides: recent progress in nanosheets, Z. Phys. Chem. 233 (2019) 117–165, https://doi.org/10.1515/zpch-2018-1125.

[49] E. Oz, S. Demirel, S. Altin, E. Altin, O. Baglayan, A. Bayri, S. Avci, Fabrication of Ca-Mn-Nb-O compounds and their structural, electrical, magnetic and thermoelectric properties, Mater. Res. Express 5 (2018), 036304, https://doi.org/10.1088/2053-1591/aab3af.

[50] D. Sedmidubský, V. Jakeš, O. Jankovský, J. Leitner, Z. Sofer, J. Hejtmánek, Phase equilibria in Ca–Co–O system, J. Solid State Chem. 194 (2012) 199–205, https://doi.org/10.1016/j.jssc.2012.05.014.

[51] G. Constantinescu, S.M. Mikhalev, A.D. Lisenkov, D.V. Lopes, A.R. Sarabando, M. C. Ferro, T.F.d. Silva, S.A. Sergiienko, A.V. Kovalevsky, Prospects for electrical performance tuning in $Ca_3Co_4O_9$ materials by metallic Fe and Ni particles additions, Materials 14 (2021), https://doi.org/10.3390/ma14040980.

[52] T. Osaka, H. Takahashi, H. Sagayama, Y. Yamasaki, S. Ishiwata, High-pressure synthesis of an unusual antiferromagnetic metal $CaCoO_3$ with $GdFeO_3$-type perovskite structure, Phys. Rev. B 95 (2017), https://doi.org/10.1103/PhysRevB.95.224440.

[53] K. Fujie, S. Horii, I. Matsubara, W. Shin, N. Murayama, J. Shimoyama, K. Kishio, Effect of high valence metal doping on thermoelectric properties of $[Ca_2CoO_{3-\delta}]_{0.62}CoO_2$, MRS Proceedings 793 (2003), https://doi.org/10.1557/PROC-793-S8.34.

[54] C.-H. Lim, W.-S. Seo, S. Lee, Y.S. Lim, J.-Y. Kim, H.-H. Park, S.-M. Choi, K.H. Lee, K. Park, Anisotropy of the thermoelectric figure of merit (ZT) in textured $Ca_3Co_4O_9$ ceramics prepared by using a spark plasma sintering process, J. Kor. Phys. Soc. 66 (2015) 794–799, https://doi.org/10.3938/jkps.66.794.